# Increasing Single-Mode Power in VCSELs With Antiresonant Oxide Island

Marta Więckowska and Maciej Dems

*Abstract*—This article focuses on increasing the single-mode power in Vertical Cavity Surface Emitting Lasers (VCSELs) through the strategic integration of an antiresonant oxide islands. Using a gallium arsenide-based VCSEL as a case study, we explore the influence of oxide island parameters on lateral mode discrimination in term of threshold currents and emitted powers. The analysis confirms non-uniform variations in threshold currents, with varying oxide island position and size. Leveraging the spatial hole burning effect, we compute the output power and identify optimal island configurations for maximizing single-mode power. The results showcase the efficacy of antiresonant oxide islands in significantly enhancing single-mode power output in VCSELs.

*Index Terms*—VCSEL, ARROW, oxidation, antiresonance, waveguiding, optical modeling, electrical modeling, spatial hole burning.

## I. INTRODUCTION

VERTICAL Cavity Surface Emitting Lasers (VCSELs) are nowadays a pivotal technology in diverse applications due to their unique advantages, such as low power consumption, high modulation bandwidth, and excellent beam quality. In the field of data communication, VCSELs play a crucial role in short-distance optical interconnects, offering high-speed and energy-efficient solutions for data transmission [1], [2]. Moreover, VCSELs find application in emerging technologies like 3D sensing, where their compact size and fast modulation capabilities contribute to the development of advanced depth-sensing systems for applications in facial recognition and augmented reality [3], [4], [5], [6]. Additionally, VCSELs have demonstrated promise in medical imaging applications, showcasing their potential in non-invasive diagnostics and imaging modalities [7], [8].

A particular significance in various applications is held by single-mode VCSELs, owing to their ability to produce a stable, well-defined output beam, which is crucial for precision-demanding tasks. In optical communication systems, the use of single-mode VCSELs enhances signal integrity and enables higher data rates over longer distances by mitigating issues associated with modal dispersion. The inherent coherence and narrow linewidth of single-mode VCSELs are advantageous for applications such as frequency-domain sensing, where high spectral purity is essential for accurate measurements. In this context, exploring the unique capabilities of single-mode VCSELs becomes paramount for advancing various fields reliant on precise and controlled optical outputs. Unfortunately, the simplest method of achieving single-mode operation of VCSELs, namely the reduction of their aperture size [9], [10], [11], is applicable only for low-power devices [12], [13], [14], as small apertures result in increased differential resistivity, higher current densities, and stronger heating [15].

To overcome this limitation, researches investigate a number of indirect approaches, like use of graphene-bubble dielectric distributed Bragg reflectors (DBRs) [16], double cavities [15], [17], shallow relief [18], zinc-diffusion with oxide-relief [19], [20], grating couplers [21], [22], [23], or application of antiresonant reflecting optical waveguides (ARROWs) [24], [25], [26], [27]. This simplest form of such antiresonant structure (S-ARROW) is a low-index core surrounded by a single high-index ring. Such S-ARROW with a core diameter of 8–12 $\mu$m has already provided a substantial mode discrimination in 980-nm VCSELs [28], [29], [30], [31], [32], [33], [34].

In our previous works, we have proposed such an S-ARROW structure for improving lateral modes discrimination in VCSELs. This structure has a form of an oxide disk manufactured in aluminum-rich AlGaAs layer inside of a VCSEL structure, either directly in the resonant cavity [35] or in one of the DBR layers [36]. This is possible through the use of a novel planar oxidation technology [37], [38], which allows to partially oxidize the AlGaAs layer through a small hole etched in the a GaAs layer covering it, before the rest of the structure is grown.

The steps to manufacture such buried oxidation are as follows: First, the epitaxial structure is grown up to the first layer covering the aluminum-rich AlGaAs, where the oxidation is to be placed. Next, a small hole is etched in the covering layer, and the wafer is placed in a wet environment where the AlGaAs oxidizes. After this, either dielectric layers are deposited to form the top DBRs or another epitaxial process is performed to grow the remaining semiconductor DBR layers. Finally, the standard VCSEL post-processing is conducted.

We call a buried oxidized structure, manufactured in such a way, an *oxide island*, as it is well localized round oxide region surrounded by other VCSEL layers. To our knowledge, it has not been investigated before by other groups. However, it has a strong impact on the profiles for lateral modes, which is examined in details in our previous articles as well as in this one. Because each mode responds qualitatively differently to the antiresonant island, this opens new possibilities for increasing
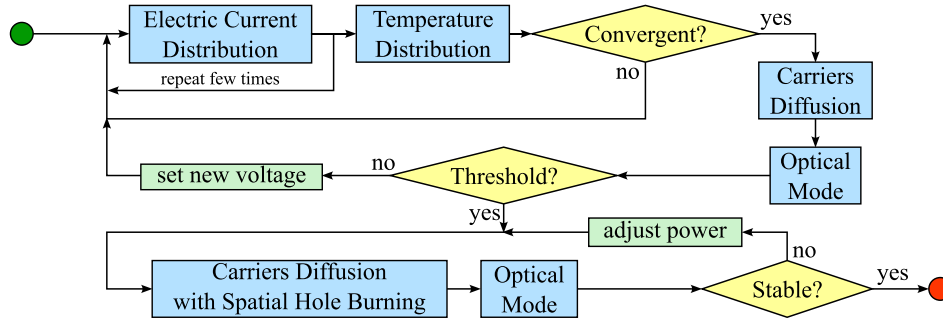
Fig. 1.    Block diagram of numeric algorithm used.

modal loss differences between them and to obtain a single-mode emission. We have already shown that optical losses of different lateral modes of a laser do not change monotonically with the island size, but are of an oscillatory nature [35]. We proved that these oscillations are caused by the distorting effect of the island, which has a low-refractive-index, on the spatial profiles of the modes. For low island sizes, the modes have a tendency to focus on the high-effective-index region outside its radius, while with larger islands they are confined within it. Later, we have shown that the threshold currents of an electrically pumped device shows the same behavior [36] and its origin closely related to the oscillations of the optical losses and is only weakly modified by the overlap of the optical mode and pumping current profile.

The mentioned analyses allowed us to estimate the potential parameters of the oxide island (namely its size and location) that provided effective discrimination of the thresholds of high-order lateral modes combined with a reasonably low threshold current of the fundamental mode. For the reader's convenience, we summarize these findings in this article and extend the performed analysis for a broader range of parameters. Then, we use them as a foundation for the new detailed analysis of the emitted output power, with particular consideration of the impact of the oxide island on the slope efficiency. This allows us to identify the island parameters that provide the maximum possible single-mode power.

## II. METHODOLOGY

Comprehensive modeling of semiconductor lasers necessitates a holistic approach, considering the mutual interactions between various physical effects, including current flow, heat dissipation, and electromagnetic wave propagation. The methodology details are outlined in [39], with an algorithm overview provided in Fig. 1. The computational process initiates by determining electric current flow, coupled self-consistently with the assessment of temperature distribution throughout the structure. Heat transfer is modeled using the finite element method, accounting for temperature-dependent thermal conductivities, necessitating a self-consistent iterative loop. Additionally, due to the semiconductor junction's presence, establishing the current density distribution requires an iterative procedure, often involving a significantly larger number of iterations than those for considering nonlinear thermal effects. As a result,

thermal and electrical computations can be interleaved, updating the temperature distribution every 10–20 electrical iterations until convergence, where both current density and temperature distributions stabilize [40].

Upon convergence, the carrier density profile $n$ in the active region is determined using the diffusion equation

$$D\,\Delta n + S - L = 0, \qquad (1)$$

where $D$ is the ambipolar diffusion coefficient, $S$ denotes current injection sources, and $L$ represents carrier losses. The injection source is related to the current density perpendicular to the active region $j_\perp$:

$$S = \frac{j_\perp}{e\,d}, \qquad (2)$$

where $e$ is the elementary charge and $d$ is the active region thickness. Carrier losses arise from three recombination processes (monomolecular, bimolecular, and Auger) and are expressed as

$$L = An + Bn^2 + Cn^3. \qquad (3)$$

Solving these equations yields the carrier density profile and information about quasi Fermi levels in the quantum wells, which can be translated into optical gain. The optical gain, represented as the imaginary part of the complex refractive index, facilitates the determination of hot-cavity optical modes. The effective frequency method [41] is employed for this purpose due to its speed and sufficient accuracy, as validated against accurate modal methods [42]. The previously determined temperature distribution allows consideration of the thermal lensing effect. However, as we show later, this effect is significant only at high currents, while for low and moderate currents, its influence on the optical modes is minor compared to that of the oxide island.

Mode thresholds are determined by ensuring the net optical loss is zero, signifying compensation of emission and absorption losses by the active region gain. For the over-threshold computation and emitted power determination, an additional carrier loss factor $L_{\text{SHB}}$, arising from the spatial hole burning (SHB) effect, is subtracted from (1). Proportional to the emitted power [43], $L_{\text{SHB}}$ is computed by requiring it to compensate for increased carriers injection resulting from higher current. However, as the spatial profile of $L_{\text{SHB}}$ is related to the optical
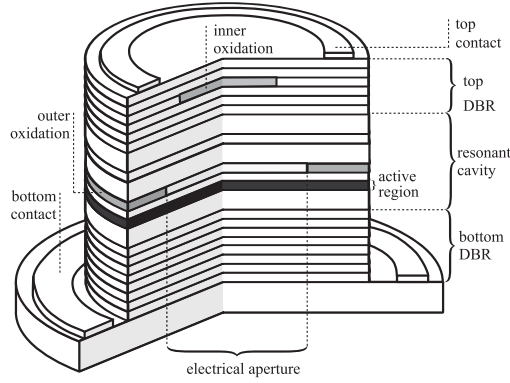
| Layer | Material | Thickness [nm] | Doping [cm$^{-3}$] |
|---|---|---|---|
| Cap | GaAs | 68.4 | C:$10^{19}$ |
| Top DBR × 24 | Al$_{0.2}$Ga$_{0.8}$As | 61.5 | C:$10^{18}$ |
| | Al$_{0.9}$Ga$_{0.1}$As | 69.9 | C:$10^{18}$ |
| Outer Oxide | Al$_{0.2}$Ga$_{0.8}$As | 39.5 | C:$10^{18}$ |
| | AlAs + AlO$_x$ | 40.0 | C:$10^{18}$ |
| Interlayer | Al$_{0.6}$Ga$_{0.4}$As | 48.0 | C:$10^{18}$ |
| Cladding | Al$_{0.3}$Ga$_{0.7}$As | 107.5 | — |
| 3 × QW | GaAs | 6.5 | — |
| 2 × Barrier | Al$_{0.3}$Ga$_{0.7}$As | 4.0 | — |
| Cladding | Al$_{0.3}$Ga$_{0.7}$As | 107.5 | — |
| Bottom DBR | Al$_{0.9}$Ga$_{0.1}$As | 69.9 | Si:$10^{18}$ |
| × 32 | Al$_{0.2}$Ga$_{0.8}$As | 61.5 | Si:$10^{18}$ |
| Substrate | GaAs | | Si:$2×10^{18}$ |

Fig. 2. Schematic illustration and layers summary of the analyzed laser. The key element, which is the oxide island at the center of the laser, is marked in light gray, as is the area of external oxidation constituting the current boundary.

modes distribution, which may substantially differ from the injected current profile, another self-consistent loop is necessary to accurately estimate the emitter optical power of the investigated laser.

### III. LATERAL MODES THRESHOLD DISCRIMINATION

Utilizing the aforementioned methodology, we scrutinize a structure illustrated in Fig. 2. This VCSEL, based on gallium arsenide, was previously analyzed in our work [36]. The resonant cavity is tailored to the free-space wavelength of 850 nm and boasts a length of $3/2\,\lambda$. Within the cavity lies an active region comprising three 6.5-nm-thick GaAs quantum wells separated by 4-nm-thick AlGaAs barriers. Positioned above the quantum wells is a 10 $\mu$m electrical aperture formed by an oxidized external AlAs area. The top of the cavity features 24 pairs of silicon-doped n-type Distributed Bragg Reflectors (DBRs), while beneath the cavity, there are 24 pairs of carbon-doped p-type DBRs. Both mirrors are composed from Al$_{0.2}$Ga$_{0.8}$As/Al$_{0.9}$Ga$_{0.1}$As layers, while both top and bottom ring contacts are crafted from gold.

The antiresonant element, the oxidized central island, resides within the subsequent layers of the top DBRs. This element serves as a crucial component of the structure, influencing mode shape, lifetime, and thereby causing the modal discrimination phenomenon [35]. For the analysis presented in this article, we
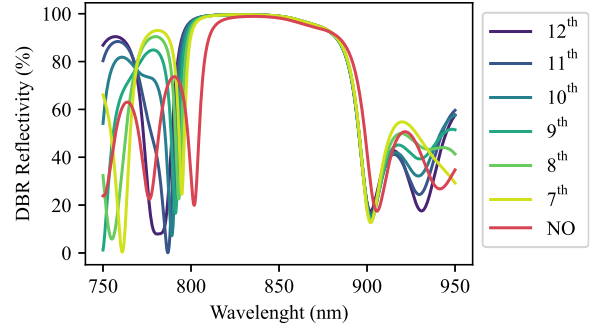


Fig. 3. Top DBR reflectivity with the oxide island located in 7th through 12th DBR pair and with no island for reference (red line, indicated "NO" in the legend).

systematically vary the size and position of the island across the area of the top DBRs layers.

The top DBRs of the structure deviate slightly from the typical $1/4$-$\lambda$ scheme. Introduction of the oxide island reduces this deviation, leading to an increase in the high-reflectivity bandwidth, as depicted in Fig. 3. Regardless of the island's position, the stop-band widens slightly for wavelengths below 800 nm, and the reflectivity remains unaffected between 800 and 900 nm. Changes induced by the oxide island primarily affect the Fabry-Perot resonance outside of the stop-band. Therefore, the primary impact of the island on the laser modes of various orders is scattering caused by the island's finite size.

Single-mode operation is most likely achieved in a structure that exhibits the highest discrimination in threshold current. This implies that one mode, usually the fundamental mode, possesses a reasonably low threshold, while all other modes require the highest possible threshold current. This discrimination is quantified by a relative threshold difference as

$$D = \frac{I_{th}^{competing} - I_{th}^{lasing}}{I_{th}^{lasing}}, \qquad (4)$$

where $I_{th}^{lasing}$ is the threshold current of the lasing mode (i.e., with the lowest threshold among all modes), and $I_{th}^{competing}$ is the threshold current of the competing mode, i.e., the one with the second lowest threshold current. This value is depicted in Fig. 4 (left axes). In each case presented, the oxide island is placed in the indicated top DBR pair, counted from the cavity (i.e., the larger the number, the farther the island is located from the cavity). The island diameter is marked on the horizontal axis, with the outer aperture consistently maintained at 10 $\mu$m.

For most oxide island sizes and positions, the lasing mode is LP$_{01}$, indicated by the red color of the thick solid line in Fig. 4. However, for certain diameters, the LP$_{02}$ mode exhibits the lowest threshold and should be considered as the primary lasing mode. This is denoted by the blue color in the discrimination plot. The competing modes may vary, and while it is not critical which one would start lasing second, this information is not indicated visually. However, it can be inferred by comparing the threshold currents marked by the dashed lines in Fig. 4.

Fig. 4 clearly illustrates that the threshold current for each mode varies non-uniformly with the oxide island diameter.
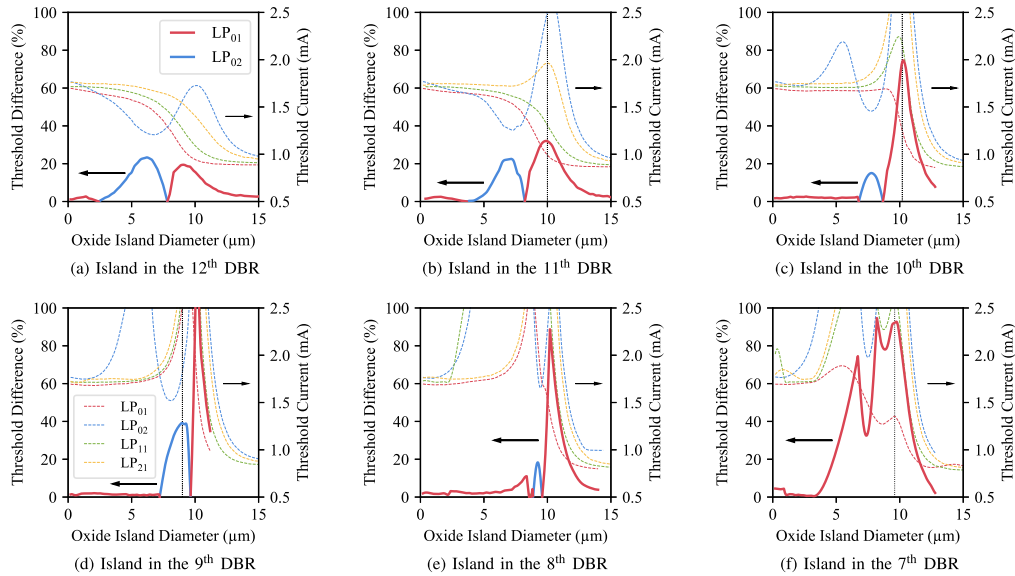
Fig. 4. Relative differences between the two lowest threshold currents for varying diameters of the oxide island and its location in the DBR layers. The thick solid lines (referring to the left axis) indicate the $D$ value, as computed with (4). Their color corresponds to the modes with the lowest thresholds (lasing modes). The colored thin dashed lines denote threshold currents of the four main modes (indicated on the right axis). The vertical dotted black lines in (b), (c), (d), and (f) mark the sizes of island, for which the modal discrimination is approximately the strongest. Structures with these parameters are investigated further in this article.

The effect is stronger when the island is located closer to the cavity. This behavior results from the match or mismatch between the modal profile and the anti-resonant oxide aperture [35], [36]. Consequently, there is a significant increase in threshold current discrimination for specific combinations of island position and diameter (marked in Fig. 4 with black dotted vertical lines). These combinations represent potential candidates for providing single-mode emission.

An important consideration is that the presented thresholds are computed individually for each mode and do not account for modal competition and hole burning effects. This results in an estimated relative threshold current difference smaller than observed in a real device, where lasing modes reduce the number of carriers available for competing modes, consequently increasing their threshold. The extent of this increase depends on the slope efficiency of the lasing mode and its overlap with the competing one, topics that are discussed further in this article.

## IV. COMPUTING OUTPUT POWER

The computation of output power involves incorporating the spatial hole burning effect into (3). Our equation assumes a steady state, requiring that the stimulated recombination rate remains independent of time. This assumption is valid in VCSELs, where modal distribution is primarily determined by the structure, ensuring stability–modes do not change over time. In the case of single-mode operation, the stimulated emission losses are defined as [39]:

$$L_{\text{SHB}}(\mathbf{r}) = P \frac{2\, g(\mathbf{r})\, M(\mathbf{r})}{(1-R)\, \hbar\omega\, \int_A M(\mathbf{r})}, \tag{5}$$

where $P$ is the mode output power, $g(\mathbf{r})$ is the optical gain distribution, $M(\mathbf{r})$ is the mode profile, $R$ is the reflectivity of DBR mirrors, and $\hbar\omega$ is the photon energy. To determine the output

power, the $L_{\text{SHB}}$ component needs to be added to the total losses in the diffusion equation. For a given voltage $U$ determining the temperature and carrier distribution, a value of $P$ is found such that the imaginary part of the modal eigenfrequency is 0, indicating zero net gain and stable emission.

The positions and diameters of oxide islands that yield the most significant discrimination in uncoupled threshold current are highlighted in Fig. 4 (panels b, c, d, and f) with vertical black dotted lines. Let's first examine the case of a 10.0-$\mu$m island located in the 11th DBR pair (Fig. 5(a)). In this scenario, the threshold for the lasing LP$_{01}$ mode is 1.0 mA. Beyond this threshold, the emitted power increases roughly linearly. The competing LP$_{11}$ mode maintains a negative net gain, remaining below the threshold until 2.124 mA, a significantly higher value than the uncoupled threshold current of 1.3 mA shown in Fig. 5(b). Consequently, the laser operates in a single-mode regime up to 2.1 mA, corresponding to an emitted power of 0.9 mW.

A similar analysis was conducted for the structure with a 10.2-$\mu$m oxide island in the 10th DBR pair (Fig. 5(b) with thresholds shown in Fig. 4(c)). The overall behavior mirrors the previous case; however, the competing mode reaches positive gain at a much higher current of 3.75 mA, resulting in a substantially higher single-mode emitted power of 2.9 mW. This is a direct consequence of the much larger original threshold discrimination for the island located closer to the cavity.

We also explored island parameters that allow the LP$_{02}$ mode to become the lasing one (Fig. 4(d)). Although the competing LP$_{01}$ mode starts lasing at a relatively high current of 2.6 mA, the LP$_{02}$ mode exhibits a significantly smaller slope efficiency than LP$_{01}$ (compare Fig. 5(c) with any other subplot of Fig. 5). As a consequence, the single-mode output power remains below 0.3 mW.

(a) 10.0-μm island in 11th DBR pair



(b) 10.2-μm island in 10th DBR pair



(c) 9-μm island in 9th DBR pair

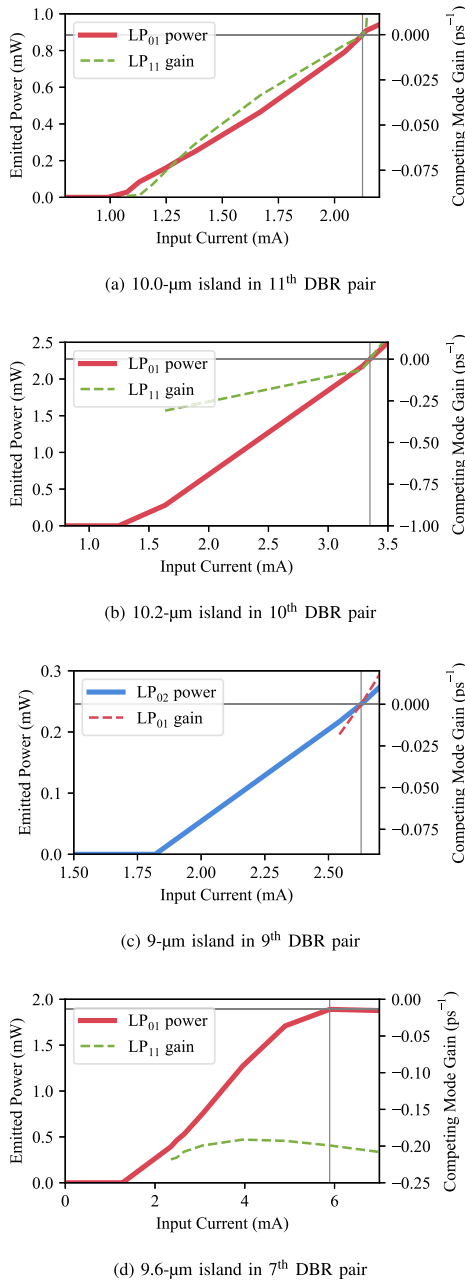

(d) 9.6-μm island in 7th DBR pair

Fig. 5. Lasing mode powers (thick solid lines) and competing mode decays (dashed lines) as a function of the input current for selected oxide island sizes and positions. Colors of the lines indicate the lasing and competing modes. Gray vertical line indicate maximum single-mode current and the horizontal one maximum single-mode emitter power. Mind that each plot have different scale on both horizontal and vertical axes.

An intriguing scenario arises for the island located in the 7th DBR pair (Fig. 5(d) corresponding to the thresholds in Fig. 4(f)). In this case, the competing mode never reaches the threshold, resulting in the laser operating in a single-mode throughout its operational range. However, due to the proximity of the island to the cavity, which increases the diode resistance [36], the slope efficiency is not large, and the roll-over of the emitted power occurs at a value of 1.9 mW.

The reason for this behavior lies in the impact of the oxide layer on current spreading and, consequently, the resistance of the VCSEL structure. As demonstrated in our previous paper [36], the closer the island is positioned to the cavity, the more it obstructs current flow, effectively increasing resistance. Therefore, an island situated farther away from the cavity (such as in the 10th DBR pair, as discussed earlier) offers improved laser performance, providing ample space for current dispersion. Similarly, the farther the island is from the cavity, the lesser its impact on the structure's capacitance, which for an analyzed VCSEL is around 0.3 pF regardless of the island presence and position.

Four investigated lasing modes have their profiles affected by the oxide island. These profiles are shown in Fig. 6. The 10-μm island located in the 11th DBR pair does not affect the shape of the lasing $LP_{01}$ mode (Fig. 6(a)). The light intensity has a Gaussian profile that perfectly fits the aperture. Also, in the case of the island located in the 10th DBR pair, the intensity maximum is located within the aperture. However, there are visible intensity lobes outside of it. The reason for their appearance is the fact that the island has a larger thickness than the outer oxidation and it spans between the node and anti-node of the standing wave (while the outer oxidation is located in the node). Hence, the effective index of the island area is smaller than that of the cladding, and we have a typical anti-waveguiding scenario.

The $LP_{02}$ mode in Fig. 6(c) has a strong peak in the center and another lobe at the island boundary, as the light tends to locate as much as possible in the narrow gap between the end of the oxide island and the outer aperture. However, the most atypical is the $LP_{01}$ mode for the island located in the 7th DBR pair (Fig. 6(d)). In this case, the mode profile strongly deviates from its classical shape, as the island effectively pushes it to the outer region. This behavior is typical for a VCSEL with an anti-resonant island and is the main cause of the strong threshold current oscillation in Fig. 4(f). It has been investigated in detail in [35].

To illustrate the effect of spatial hole burning induced by the lasing mode on the competing mode, we present the gain profiles for a 10.2-μm oxide island in the 10th DBR pair in two cases: the original gain resulting from carrier concentration computed with the unmodified equation (1) and the one with burned carriers at 3.8 mA current (i.e., the maximum single-mode power) in Fig. 7. The burned profile is generally much lower and does not follow the light intensity profile due to strong carrier diffusion.

The summarized results of the investigated cases are presented in Table I. The table indicates the position and diameter of the oxide island, specifies which modes are identified as the lasing and competing ones, and provides the threshold current for the lasing mode, along with both uncoupled and coupled threshold currents for the competing mode. The final column displays the maximum single-mode power emitted by the laser, reaching its highest value of 2.9 mW for the 10.2-μm island located in the 10th DBR pair. While this may not set a record compared to values obtained with anti-resonant elements [44], it unequivocally demonstrates the effectiveness of the oxide island in enhancing the single-mode power emitted by VCSELs.

(a) LP$_{01}$ mode with the 10.0-μm island in 11$^{th}$ DBR pair

(b) LP$_{01}$ mode with the 10.2-μm island in 10$^{th}$ DBR pair

(c) LP$_{02}$ mode with the 9-μm island in 9$^{th}$ DBR pair

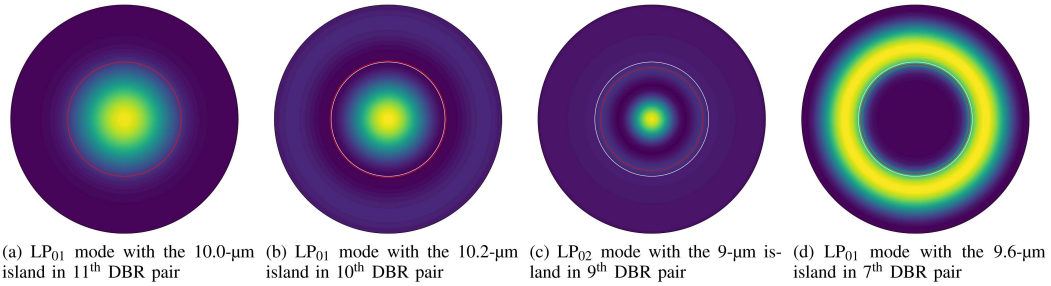(d) LP$_{01}$ mode with the 9.6-μm island in 7$^{th}$ DBR pair

Fig. 6.    Lateral profiles of the modes depicted in Fig. 5. White and red circles indicate the aperture and the size of the oxide island, respectively. Due to the presence of the island, the mode shapes do not always resemble the classical LP modes. The particulars of the differences and their origins are discussed in the main text.

TABLE I
THRESHOLD VOLTAGE CALCULATED FOR THREE SETS OF ISLAND PARAMETERS IN TWO CASES: WITH AND WITHOUT THE SPATIAL HOLE BURNING EFFECT

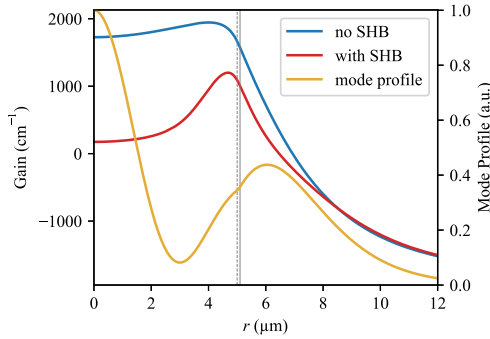| Oxide Island | | Mode lasing/competing | Threshold Current [mA] | | Max. Single-Mode Power [mW] |
|---|---|---|---|---|---|
| DBR Pair | Diameter [μm] | | No SHB | SHB | |
| 7$^{th}$ | 9.6 | LP$_{01}$ | 1.3 | | 1.9 |
| | | LP$_{11}$ | 2.4 | × | |
| 9$^{th}$ | 9.0 | LP$_{02}$ | 1.8 | | 0.25 |
| | | LP$_{01}$ | 2.5 | 2.6 | |
| 10$^{th}$ | 10.2 | LP$_{01}$ | 1.2 | | 2.9 |
| | | LP$_{11}$ | 1.8 | 3.8 | |
| 11$^{th}$ | 10.0 | LP$_{01}$ | 1.0 | | 0.9 |
| | | LP$_{11}$ | 1.3 | 2.1 | |



Fig. 7.    Gain profile computed without (blue line) and with (red line) considering SHB effect for a structure with 10.2-$\mu$m island in 10th DBR pair. The yellow line shows lasing mode profile that is the cause of the carriers burning.

## V. CONCLUSION

In conclusion, our investigation into the gallium arsenide-based VCSEL structure with an antiresonant oxide island has revealed promising insights for achieving single-mode operation and maximizing output power. The careful selection of the oxide island's size and position within the top DBRs significantly influences the discrimination of threshold currents, a critical factor for single-mode emission.

The presented results, depicted in Fig. 4, demonstrate a nuanced relationship between the oxide island diameter and the threshold currents for various modes. The non-uniform variation in threshold currents, particularly pronounced when the island is closer to the cavity, highlights the potential for optimizing the structure to enhance modal discrimination.

Moreover, the computation of output power, considering spatial hole burning effects, provides a theoretical foundation for understanding the power characteristics of the VCSEL. The exploration of individual modes before analyzing mutual mode interactions offers valuable insights into the behavior of the laser under different conditions.

The investigation into competing mode threshold increase further underscores the importance of the oxide island parameters in achieving single-mode operation. Specific island positions and diameters prevent competing modes from reaching the threshold, leading to enhanced single-mode emitted power. The maximum single-mode power achieved, as demonstrated for a 10.2-$\mu$m oxide island in the 10th DBR pair, attests to the efficacy of the antiresonant element in optimizing VCSEL performance.

In summary, the study advances our understanding of the role of antiresonant elements, specifically oxide islands, in shaping the modal characteristics of VCSELs. It is essential to note that while our analysis provides valuable theoretical groundwork, real-world devices may exhibit additional complexities. For this reason no rigorous optimization of the structure is presented in this article. We believe that such procedure would provide additional improvement in modal discrimination and increase maximum single-mode power. Future research should consider properties of experimentally measured device for a comprehensive understanding of VCSEL behavior and they should focus on quantitative optimization of the proposed structure. Nevertheless, our findings pave the way for further exploration and optimization of VCSEL designs to achieve enhanced single-mode operation and maximize output power in practical applications.

## REFERENCES

[1] H. Li et al., "Energy efficiency, bit rate, and modal properties of 980nm VC-SELs for very-short-reach optical interconnects," *Proc. SPIE*, vol. 9001, pp. 70–77, 2014.

[2] H. Li, P. Wolf, P. Moser, G. Larisch, J. A. Lott, and D. Bimberg, "Temperature-stable, energy-efficient, and high-bit rate oxide-confined 980-nm VCSELs for optical interconnects," *IEEE J. Select. Topics Quantum Electron*, vol. 21, no. 6, pp. 405–413, Nov./Dec. 2015.

[3] E. Watanabe, N. Takeda, and K. Kodate, "Fabrication and evaluation of a facial recognition system based on PJTC using two-dimensional VCSEL array module," *Proc. SPIE*, vol. 5005, pp. 345–356, 2003.

[4] E. Watanabe, N. Arima, and K. Kodate, "Facial recognition system with compact optical parallel correlator using vertical-cavity surface-emitting laser array module," *Jpn. J. Appl. Phys.*, vol. 43, no. 8S, Aug. 2004, Art. no. 5890.

[5] B. D. Padullaparthi, T. Tamanuki, and D. Bimberg, "Field-of-view control of segmented NIR VCSEL arrays for next-generation flash LiDARs," *Proc. SPIE*, vol. 11262, pp. 202–207, 2020.

[6] M. Dummer, K. Johnson, S. Rothwell, K. Tatah, and M. Hibbs-Brenner, "The role of VCSELs in 3D sensing and LiDAR," *Proc. SPIE*, vol. 11692, pp. 42–55, 2021.

[7] M. K. Hibbs-Brenner, K. L. Johnson, and M. Bendett, "VCSEL technology for medical diagnostics and therapeutics," *Proc. SPIE*, vol. 7180, pp. 117–126, 2009.

[8] V. Jayaraman et al., "Widely tunable electrically pumped 1050nm MEMS-VCSELs for optical coherence tomography," *Proc. SPIE*, vol. 11300, pp. 124–131, 2020.

[9] C. Jung et al., "4.8mW singlemode oxide confined top-surface emitting vertical-cavity laser diodes," *Electron. Lett.*, vol. 33, no. 21, pp 1790–1791, 1997.

[10] M. Grabherr, R. Jager, R. Michalzik, B. Weigl, G. Reiner, and K. J. Ebeling, "Efficient single-mode oxide-confined GaAs VCSEL's emitting in the 850-nm wavelength regime," *IEEE Photon. Technol. Lett*, vol. 9, no. 10, pp. 1304–1306, Oct. 1997.

[11] N. Ueki et al., "Single-transverse-mode 3.4-mW emission of oxide-confined 780-nm VCSELs," *IEEE Photon. Technol. Lett*, vol. 11, no. 12, pp. 1539–1541, Dec. 1999.

[12] G. Stepniak et al., "54 Gbit/s OOK transmission using single-mode VCSEL up to 2.2km MMF," *Electron. Lett.*, vol. 52, no. 8, pp. 633–635, 2016.

[13] R. Puerta et al., "107.5 Gb/s 850 nm multi- and single-mode VCSEL transmission over 10 and 100 m of multi-mode fiber," in *Proc. Opt. Fiber Commun. Conf. Exhib.*, 2016, pp. 1–3.

[14] Hsuan-Yun Kao et al., "Long-term thermal stability of single-mode VC-SEL under 96-Gbit/s OFDM transmission," *IEEE J. Sel. Topics Quantum Electron.*, vol. 25, no. 6, pp. 1–9, Nov./Dec. 2019.

[15] V. Shchukin et al., "Single-mode vertical cavity surface emitting laser via oxide-aperture-engineering of leakage of high-order transverse modes," *IEEE J. Quantum Electron.*, vol. 50, no. 12, pp. 990–995, Dec. 2014.

[16] B. Guan, P. Li, S. Arafin, Y. Alaskar, and K. L. Wang, "Investigation of single-mode vertical-cavity surface-emitting lasers with graphene-bubble dielectric DBR," *Photon. Nanostructures - Fundamentals Appl.*, vol. 28, pp. 56–60, Feb. 2018.

[17] N. Ledentsov et al., "Leaky cavity 850 nm single-mode VCSELs for high-speed data transmission over multi-mode fiber," in *Proc. Photon. Switching Comput. Conf.*, 2018, pp. 1–3.

[18] Å. Haglund, J. S. Gustavsson, J. Vukusic, P. Modh, and A. Larsson, "Single fundamental-mode output power exceeding 6 mW from VCSELs with a shallow surface relief," *IEEE Photon. Technol. Lett*, vol. 16, no. 2, pp. 368–370, Feb. 2004.

[19] J.-W. Shi et al., "Single-mode, high-speed, and high-power vertical-cavity surface-emitting lasers at 850 nm for short to medium reach (2 km) optical interconnects," *J. Lightw. Technol.*, vol. 31, no. 24, pp. 4037–4044, Dec. 2013.

[20] Z. Khan, J.-C. Shih, C.-L. Cheng, and J.-W. Shi, "High-power and highly single-mode zn-diffusion VCSELs at 940 nm wavelength," in *Proc. IEEE Photon. Conf.*, 2019, pp. 1–2.

[21] L. Bao et al., "Single-mode emission from vertical-cavity surface-emitting lasers with low-index defects," *IEEE Photon. Technol. Lett*, vol. 19, no. 4, pp. 239–241, Feb. 2007.

[22] M. Dems et al., "VCSEL modeling with self-consistent models: From simple approximations to comprehensive numerical analysis," *Proc. SPIE*, vol. 9381, pp. 147–155, 2015.

[23] E. Haglund et al., "High-power single transverse and polarization mode VCSEL for silicon photonics integration," *Opt. Exp.*, vol. 27, no. 13, pp. 18892–18899, Jun. 2019.

[24] Y. Kokubun, T. Baba, T. Sakaki, and K. Iga, "Low-loss antiresonant reflecting optical waveguide on SI substrate in visible-wavelength region," *Electron. Lett.*, vol. 22, no. 17, pp. 892–893, Aug. 1986.

[25] T. L. Koch, U. Koren, G. D. Boyd, P. J. Corvini, and M. A. Duguay, "Antiresonant reflecting optical waveguides for III-V integrated optics," *Electron. Lett.*, vol. 23, no. 5, pp. 244–245, Feb. 1987.

[26] D. Yin, H. Schmidt, J. P. Barber, and A. R. Hawkins, "Integrated ARROW waveguides with hollow cores," *Opt. Exp.*, vol. 12, no. 12, pp. 2710–2715, Jun. 2004.

[27] N. N. Ledentsov et al., "Anti-waveguiding vertical-cavity surface-emitting laser at 850 nm: From concept to advances in high-speed data transmission," *Opt. Exp.*, vol. 26, no. 1, pp. 445–453, Jan. 2018.

[28] Y. A. Wu, G. S. Li, R. F. Nabiev, K. D. Choquette, C. Caneau, and C. J. Chang-Hasnain, "Single-mode, passive antiguide vertical cavity surface emitting laser," *IEEE J. Sel. Topics Quantum Electron.*, vol. 1, no. 2, pp. 629–637, Jun. 1995.

[29] I. V. Goltser, L. J. Mawst, and D. Botez, "Single-cladding antiresonant reflecting optical waveguide-type diode laser," *Opt. Lett.*, vol. 20, no. 21, pp. 2219–2221, Nov. 1995.

[30] D. Zhou and Luke J. Mawst, "High-power single-mode antiresonant reflecting optical waveguide-type vertical-cavity surface-emitting lasers," *IEEE J. Quantum Electron*, vol. 38, no. 12, pp. 1599–1606, Dec. 2002.

[31] C. W. Tee and S. F. Yu, "Design and analysis of cylindrical antiresonant reflecting optical waveguide," *J. Light. Technol*, vol. 21, no. 12, pp. 3379–3386, 2003.

[32] C. W. Tee, C. C. Tan, and S. F. Yu, "Design of antiresonant-reflecting optical waveguide-type vertical-cavity surface-emitting lasers using transfer matrix method," *IEEE Photon. Technol. Lett.*, vol. 15, no. 9, pp. 1231–1233, Sep. 2003.

[33] C. W. Tee, S. F. Yu, and N. S. Chen, "Transverse-leaky-mode characteristics of ARROW VCSELs," *J. Lightw. Technol.*, vol. 22, no. 7, pp. 1797–1804, Jul. 2004.

[34] C. W. Tee, S. F. Yu, R. V. Penty, and I. H. White, "Transient response of ARROW VCSELs," *IEEE J. Quantum Electron*, vol. 41, no. 2, pp. 140–147, Feb. 2005.

[35] M. Wieckowska, T. Czyszanowski, G. Almuneau, and M. Dems, "Shaping vertical-cavity surface-emitting laser mode profiles with an antiresonant oxide island for improved single-mode emission," *J. Opt. Soc. Amer. B*, vol. 35, no. 9, 2018, Art. no. 2259.

[36] M. Wieckowska, R. P. Sarzała, R. Ledzion, and M. Dems, "Impact of an antiresonant oxide island on the lasing of lateral modes in VCSELs," *Materials*, vol. 13, no. 9, Jan. 2020, Art. no. 2195.

[37] C. Amat et al., "Free engineering of buried oxide patterns in GaAs/AlAs epitaxial structures," *Electron. Lett*, vol. 43, no. 13, pp. 730–732, 2007.

[38] F. Chouchane, J. B. Doucet, A. Arnoult, G. Lacoste, C. Fontaine, and G. Almuneau, "A new approach of planar oxidation of buried al xGa 1-xAs/GaAs epitaxial structures for optical and electrical confinement applications," *Phys. Status Solidi Curr. Top. Solid State Phys.*, vol. 9, no. 2, pp. 338–341, 2012.

[39] R. Sarzała et al., "Numerical self-consistent analysis of VCSELs," *Adv. Opt. Technol.*, vol. 2012, 2012, Art. no. 689519.

[40] Łukasz Piskorski, Robert P. Sarzała, and Włodzimierz Nakwaski, "Self-consistent model of 650 nm GaInP/AlGaInP quantum-well vertical-cavity surface-emitting diode lasers," *Semicond. Sci. Technol*, vol. 22, no. 6, pp. 593–600, 2007.

[41] H. Wenzel and Hans Jürgen Wünsche, "The effective frequency method in the analysis of vertical-cavity surface-emitting lasers," *IEEE J. Quantum Electron*, vol. 33, no. 7, pp. 1156–1162, Jul. 1997.

[42] M. Wieckowska, M. Dems, and T. Czyszanowski, "Comparison of methods for simulation of the optical properties of VCSELs," *Sci. Bull. Phys.*, vol. 38, pp. 71–80, 2018.

[43] M. Wasiak, "Mathematical rigorous approach to simulate an over-threshold VCSEL operation," *Physica E: Low-Dimensional Syst. Nanostructures*, vol. 43, no. 8, pp. 1439–1444, Jun. 2011.

[44] X. F. Li, S. F. Yu, and W. J. Fan, "Design of stable single-mode chaotic light source using antiresonant reflecting optical waveguide vertical-cavity surface-emitting lasers," *IEEE J. Quantum Electron*, vol. 44, no. 4, pp. 338–345, Apr. 2008.